Multispectral intensity diffraction tomography reconstruction theory: quasi-nondispersive objects

Mark A. Anastasio and Daxin Shi

Department of Biomedical Engineering, Illinois Institute of Technology, Chicago, Illinois 60616

Greg Gbur

Department of Physics and Optical Science, University of North Carolina at Charlotte,
Charlotte, North Carolina 28223

Received June 28, 2005; revised December 12, 2005; accepted December 18, 2005; posted December 22, 2005 (Doc. ID 62994)

A multispectral intensity diffraction tomography (I-DT) reconstruction theory for quasi-nondispersive scattering objects is developed and investigated. By "quasi-nondispersive" we refer to an object that is characterized by a refractive index distribution that is approximately nondispersive over a predefined finite temporal frequency interval in which the tomographic measurements are acquired. The scanning requirements and measurement data are shown to be different than in conventional I-DT. Unlike conventional I-DT that requires intensity measurements on a pair of detector planes for each probing wave field, this new method uses measurements on a single detector plane at two frequencies. Computer simulation studies are conducted to demonstrate the method. © 2006 Optical Society of America

OCIS codes: 290.3200, 110.6960, 120.5050.

1. INTRODUCTION

Diffraction tomography[1,2] (DT) is a linearized inverse scattering method for determination of the complex-valued refractive index distribution of an object. The potential applications of DT are numerous, and include a variety of imaging problems in optics,[3–5] coherent x-ray imaging,[6,7] and acoustics.[8,9] DT can be viewed as a generalization of conventional x-ray computed tomography (CT) in which a time-harmonic coherent wave field is used to probe the object and certain first-order coherent scattering effects are accounted for. However, unlike in x-ray CT where the projection data represent intensity measurements, DT imaging requires knowledge of the phase and amplitude of the transmitted wave fields. Although wave field phase measurements can sometimes be performed experimentally when imaging with low-frequency wave fields, they introduce well-known experimental difficulties[3] in high-frequency imaging applications that arise in optics.

A new version of DT, which we have termed[10,11] intensity DT (I-DT), has been proposed in recent years by Gbur and Wolf.[12,13] I-DT circumvents the need to measure the transmitted wave field phase by requiring two or more measurements of wave field intensity in different parallel detector planes at each tomographic view angle. In essence, the I-DT reconstruction theory performs an implicit noninterferometric phase retrieval during the process of recovering the scattering potential. This is possible because of the extra degree of freedom in the measurement data afforded by the second intensity measurement, and is conceptually similar to explicit phase retrieval approaches based on the transport-of-intensity equation.[14,15]

The success of I-DT rests in the ability to extract a pair of distinct equations for a pair of Fourier components of the scattering object by the use of two intensity measurements at different distances from the scatterer. The use of multiple measurement planes introduces an additional, potentially undesirable, degree of complexity to the problem. It is reasonable to expect, however, that any change in the measurement system that results in two distinct measurements related to object structure for a single direction of incidence would be similarly successful. One possibility is to use multiple temporal frequencies for each measurement direction, but this is restricted by the fact that the scattering properties of an object are typically frequency dependent (i.e., the object is dispersive). If the scattering properties of the object are effectively constant over the range of frequencies used to probe the object, however, useful information can potentially be extracted.

In this paper, a multispectral I-DT reconstruction theory for quasi-nondispersive, linear, isotropic scattering objects is developed and investigated. By quasi-nondispersive we refer to an object that is characterized by a refractive index distribution that is approximately independent of temporal frequency over a defined finite closed interval in which the tomographic measurements are acquired. If this temporal frequency interval is chosen short enough and is placed sufficiently far from resonance frequencies of the medium, a wide class of objects can satisfy this definition. The salient feature of our reconstruction theory is that it requires two intensity measurements to be acquired on a single detector plane behind the object, where each measurement must correspond to a probing wave field with distinct frequency that resides within the quasi-nondispersive temporal frequency interval. This permits the frequency, or wavelength, of the probing

1084-7529/06/061359-10/$15.00 © 2006 Optical Society of America

wave field to be varied for acquisition of the necessary measurement data, rather than the detector placement as required in conventional I-DT. In addition to being of theoretical interest, such a data-acquisition strategy may have significant practical advantages in certain imaging studies. It is worth noting that a similar strategy has been used in anomalous x-ray scattering,[16] in which the frequency-independent partial structure factors of a multispecies liquid are extracted by measurements of the scattered field at multiple frequencies. Similarly, single species structure factors have been extracted using limited view angles and polychromatic light.[17]

The paper is organized as follows. In Section 2 we review the salient features of conventional I-DT reconstruction theory that provide a basis for our analysis. In Section 3, Fourier space data symmetries are identified, which are utilized in the development of two novel reconstruction methods in Section 4. A demonstration of the methods that utilizes computer simulation data is presented in Section 5, and a discussion and summary of the work is provided in Section 6.

2. BACKGROUND

The coordinate system given in Fig. 1 is utilized to describe the tomographic scanning geometry shown in Fig. 2. The rotated Cartesian coordinate system $\mathbf{r}=(x,y_r,z_r)$ is related to a reference system $\mathbf{r}=(x,y,z)$ by a rotation about the x axis, which represents the axis of tomographic scanning, such that $y_r=y\cos\phi+z\sin\phi$ and $z_r=z\cos\phi-y\sin\phi$. The angle ϕ is measured from the positive y axis and describes the tomographic view angle. The unit vectors $\mathbf{s}_1$, $\mathbf{s}_{2,r}(\phi)$ and $\mathbf{s}_{0,r}(\phi)$ are used to indicate the directions of the positive x, y_r and z_r axes, respectively. In terms of these coordinates, at a given view angle ϕ, $\mathbf{s}_{0,r}$ denotes the direction of the optical axis and $z_r=d$ represents the detector plane that is perpendicular to it. Note that when the tomographic view angle ϕ is varied, the optical axis and detector plane rotate simultaneously about the x axis.

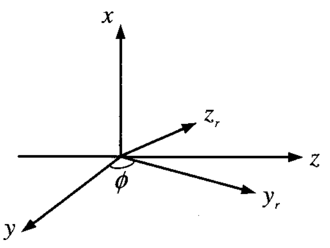

Fig. 1. Rotated coordinate system used to describe the tomographic measurement geometry.

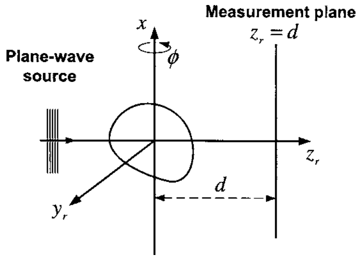

Fig. 2. In the measurement geometry, a plane wave with wavenumber k_1 irradiates the object, and the intensity of the forward-scattered wave field is measured on the plane $z_r=d$. The measurement is repeated using an incident plane wave with wavenumber k_2. Tomographic scanning is achieved by simultaneously rotating the source and detector plane about the x axis.

We will assume that a plane wave $U_i(\mathbf{r};\omega)=\exp(ik\mathbf{s}_{0,r}\cdot\mathbf{r})$ is incident at a view angle ϕ on an object that is contained within a finite volume V. The time dependence $\exp(i\omega t)$ is assumed, and $k\equiv\omega/c_0$ denotes the wavenumber where c_0 is the constant speed of light in the homogeneous and lossless background medium. Assuming that the scattering is sufficiently weak, the total wave field behind the object can be expressed by use of the first Rytov approximation as[1]

$$U(\mathbf{r};\omega)\approx U_i(\mathbf{r};\omega)\exp[\psi(\mathbf{r};\omega)], \tag{1}$$

where the complex phase is given by

$$\psi(\mathbf{r};\omega)=\frac{k^2}{4\pi U_i(\mathbf{r};\omega)}\int_V \mathrm{d}^3\mathbf{r}' f^{\omega}(\mathbf{r}')U_i(\mathbf{r}';\omega)\frac{\exp(ik|\mathbf{r}-\mathbf{r}'|)}{|\mathbf{r}-\mathbf{r}'|}, \tag{2}$$

and

$$f^{\omega}(\mathbf{r})\equiv n^2(\mathbf{r};\omega)-1. \tag{3}$$

The scattering potential $f^{\omega}(\mathbf{r})$ describes the complex-valued refractive index distribution $n(\mathbf{r};\omega)$ of the object. The superscript on $f^{\omega}(\mathbf{r})$ indicates its functional dependence on the temporal frequency of the probing wave field. It should be noted that our definition of the scattering potential in Eq. (3) differs from the conventional definition[1,13] by a factor of $k^2/4\pi$, which we have placed outside the integral in Eq. (2).

In I-DT, the measurement data are given by the wave field intensities rather than the complex amplitudes, which are assumed to be measurable in DT. To make explicit the dependence of the wave field quantities on the tomographic view angle, we will let $U(x,y_r;d,\phi,\omega)$ and $\psi(x,y_r;d,\phi,\omega)$ denote the total wave field and complex phase, respectively, on the detector plane $z_r=d$ when the experiment is conducted at view angle ϕ. The intensity measured on the detector plane at this view angle is described by

$$\begin{aligned} I(x,y_r;d,\phi,\omega)&=|U(x,y_r;d,\phi,\omega)|^2\\ &=\exp[\psi(x,y_r;d,\phi,\omega)+\psi^*(x,y_r;d,\phi,\omega)], \end{aligned} \tag{4}$$

where $*$ denotes complex conjugation. It proves useful to introduce the intensity data function

$$\begin{aligned} D(x,y_r;d,\phi,\omega)&=\log[I(x,y_r;d,\phi,\omega)]\\ &=\psi(x,y_r;d,\phi,\omega)+\psi^*(x,y_r;d,\phi,\omega). \end{aligned} \tag{5}$$

The quantities

$$\begin{aligned} \hat{D}(u,v_r;d,\phi,\omega)=\frac{1}{(2\pi)^2}\int_{\infty}\int_{\infty}\mathrm{d}x\mathrm{d}y_r\,D(x,y_r;d,\phi,\omega)\\ \times\exp[-i(ux+v_ry_r)], \end{aligned} \tag{6}$$

and

$$\hat{F}^{\omega}(\mathbf{K}) = \frac{1}{(2\pi)^3}\int_V \mathrm{d}^3\mathbf{r}\, f^{\omega}(\mathbf{r})\exp[-i\mathbf{K}\cdot\mathbf{r}] \tag{7}$$

represent the two-dimensional (2D) Fourier transform of $D(x,y_r;d,\phi,\omega)$ on the plane $z_r=d$ and three-dimensional (3D) Fourier transform of $f^{\omega}(\mathbf{r})$, respectively. Here, the variables (u,v_r) represent the spatial frequencies of the 2D data function, while the vector $\mathbf{K}$ represents the spatial frequencies of the 3D scattering potential. For the remainder of this paper, spatial frequencies will simply be referred to as frequencies. It has been demonstrated[12,13] that the intensity data function and scattering potential are related by the equation

$$\hat{D}(u,v_r;d,\phi,\omega) = i\frac{\pi k^2}{\nu}\{\hat{F}^{\omega}[u,v_r;\phi,\omega]\exp[i(\nu-k)d] - (\hat{F}^{\omega}[-u,-v_r;\phi,\omega])^{*}\exp[-i(\nu-k)d]\}, \tag{8}$$

where

$$\hat{F}^{\omega}[u,v_r;\phi,\omega] \equiv \hat{F}^{\omega}(u\mathbf{s}_1 + v_r\mathbf{s}_{2,r}(\phi) + (\nu-k)\mathbf{s}_{0,r}(\phi)), \tag{9}$$

$$\nu \equiv \sqrt{k^2-u^2-v_r^2}, \tag{10}$$

and where we recall that $k=\omega/c_0$. To clarify this notation, note that the superscript ω on $\hat{F}^{\omega}[u,v_r;\phi,\omega]$ denotes that the definition of the scattering potential depends on ω (for dispersive objects), while the parameter ω in the argument denotes that the set of frequency components at which $\hat{F}^{\omega}[\cdot]$ is evaluated also depends on ω. Stated otherwise, for a fixed ϕ, the domain of the 2D function $\hat{F}^{\omega}[u,v_r;\phi,\omega]$ corresponds to the surface of a shifted Ewald hemisphere with radius $k=\omega/c_0$. In this work, we assume that $u^2+v_r^2\leqslant k^2$ and therefore ν is real valued. This is justified because we do not aim to reconstruct frequency components of the object that are carried by evanescent wave modes.[18]

3. QUASI-NONDISPERSIVE OBJECTS AND FOURIER SPACE SYMMETRIES

A. Quasi-Nondispersive Objects

Consider that at each view angle ϕ the two intensity measurements $I(x,y_r,d;\phi,\omega_1)$ and $I(x,y_r,d;\phi,\omega_2)$ are acquired on the detector plane $z_r=d$ by use of the probing wave fields $U_i(\mathbf{r};\omega_1)$ and $U_i(\mathbf{r};\omega_2)$, respectively, where $\omega_1>\omega_2$. According to Eqs. (5) and (8), $I(x,y_r;d,\phi,\omega_1)$ and $I(x,y_r;d,\phi,\omega_2)$ are related to linear combinations of frequency components of the scattering potentials $f^{\omega_1}(\mathbf{r})$ and $f^{\omega_2}(\mathbf{r})$, respectively. In general, these measurements do not permit reconstruction of either $f^{\omega_1}(\mathbf{r})$ or $f^{\omega_2}(\mathbf{r})$. Let us assume that the frequencies ω_1 and ω_2 reside within a temporal frequency interval over which the object can be regarded as dispersionless. In this case we have

$$f(\mathbf{r}) \equiv f^{\omega_1}(\mathbf{r}) = f^{\omega_2}(\mathbf{r}), \tag{11}$$

$$\hat{F}[u,v_r;\phi,\omega_1] = \hat{F}^{\omega_1}[u,v_r;\phi,\omega_1], \tag{12}$$

$$\hat{F}[u,v_r;\phi,\omega_2] = \hat{F}^{\omega_2}[u,v_r;\phi,\omega_2], \tag{13}$$

where $\hat{F}[\cdot]$ describes the corresponding Fourier components of $f(\mathbf{r})$. Let $k_j\equiv\omega_j/c_0$ and

$$\nu_j \equiv [k_j^2-u^2-v_r^2]^{1/2}, \tag{14}$$

where $j=1,2$ and $u^2+v_r^2\leqslant k_j^2$. By use of Eqs. (5) and (8), the intensity measurements are found to satisfy

$$\hat{D}(u,v_r;d,\phi,\omega_1) = i\frac{\pi k_1^2}{\nu_1}\{\hat{F}[u,v_r;\phi,\omega_1]\exp[i(\nu_1-k_1)d] - (\hat{F}[-u,-v_r;\phi,\omega_1])^{*}\exp[-i(\nu_1-k_1)d]\}, \tag{15}$$

for $u^2+v_r^2\leqslant k_1^2$ and

$$\hat{D}(u,v_r;d,\phi,\omega_2) = i\frac{\pi k_2^2}{\nu_2}\{\hat{F}[u,v_r;\phi,\omega_2]\exp[i(\nu_2-k_2)d] - (\hat{F}[-u,-v_r;\phi,\omega_2])^{*}\exp[-i(\nu_2-k_2)d]\} \tag{16}$$

for $u^2+v_r^2\leqslant k_2^2$. Equations (15) and (16) constitute a system of equations that relate the two intensity measurements on the detector plane $z_r=d$ at view angle ϕ to four distinct frequency components of $f(\mathbf{r})$. We demonstrate in Section 4 that this 2×4 system provides the basis for the unique reconstruction of $\hat{F}[u,v_r;\phi,\omega_2]$ for $u^2+v_r^2\leqslant k_2^2$, from which an estimate of $f(\mathbf{r})$ can be reconstructed using existing DT reconstruction algorithms.[19–21]

B. Fourier Space Symmetries

To facilitate the development of the reconstruction methods described in Section 4, we identify symmetries that relate the Fourier components $\hat{F}[u,v_r;\phi,\omega_2]$ and $\hat{F}[u,v_r;\phi,\omega_1]$ that reside on the different Ewald surfaces. The key to achieving this is the observation that, by rotating one of the Ewald surfaces about the u axis (the direction $\mathbf{s}_1$), the two surfaces can be made to intersect at prescribed locations.

It can be verified that

$$\hat{F}[u,v_r;\phi+\phi',\omega_2] = \hat{F}[u,v_r';\phi,\omega_1], \tag{17}$$

where

$$v_r' = \left[R^2 - \frac{(R^2+u^2)}{4k_1^2}\right]^{1/2}\operatorname{sgn}(v_r), \tag{18}$$

with $\operatorname{sgn}(v_r)\equiv 1$ for $v_r\geqslant 0$ and -1 otherwise, and

$$R \equiv [v_r^2 + (\nu_2-k_2)^2]^{1/2}. \tag{19}$$

The angle ϕ' is defined as

$$\phi' = -\arctan\left(\frac{v_r'}{\nu_1'-k_1}\right) + \arctan\left(\frac{v_r}{\nu_2-k_2}\right), \tag{20}$$

where ν_1' denotes ν_1 evaluated at $v_r=v_r'$, i.e.,

$$\nu_1' = [k_1^2 - u^2 - (v_r')^2]^{1/2}. \tag{21}$$

From Eq. (9), one finds that the symmetries given in Eq. (17) state simply that the vectors $\mathbf{K}_2^+ = u\mathbf{s}_1 + v_r\mathbf{s}_{2,r}(\phi+\phi') + (\nu_2 - k_2)\mathbf{s}_{0,r}(\phi+\phi')$ and $\mathbf{K}_1^+ = u\mathbf{s}_1 + v_r'\mathbf{s}_{2,r}(\phi) + (\nu_1' - k_1)\mathbf{s}_{0,r}(\phi)$ describe the same point in the 3D Fourier space of the scattering potential (see Appendix A). Equivalently, the symmetries can be understood by consideration of Fig. 3, which displays a plane of constant u in 3D Fourier space. Equation (17) states that point A on the Ewald surface of radius k_2 can be made to coincide with point B on the Ewald surface of radius k_1 by rotating the former Ewald surface by an angle $-\phi'$ about the u axis. Equation (17) states also that point C that resides on the Ewald surface of radius k_2 can be made to coincide with point D on the Ewald surface of radius k_1 by rotating the former Ewald surface by an angle ϕ' about the u axis.

Similarly, it can be verified that

$$\hat{F}[u, v_r; \phi - \phi'', \omega_2] = \hat{F}[u, -v_r'; \phi, \omega_1], \tag{22}$$

where

$$\phi'' = -\arctan\left(\frac{v_r'}{\nu_1' - k_1}\right) - \arctan\left(\frac{v_r}{\nu_2 - k_2}\right). \tag{23}$$

The symmetries given in Eq. (22) reflect that the vectors $\mathbf{K}_2^- = u\mathbf{s}_1 + v_r\mathbf{s}_{2,r}(\phi-\phi'') + (\nu_2 - k_2)\mathbf{s}_{0,r}(\phi-\phi'')$ and $\mathbf{K}_1^- = u\mathbf{s}_1 - v_r'\mathbf{s}_{2,r}(\phi) + (\nu_1' - k_1)\mathbf{s}_{0,r}(\phi)$ describe the same point in the 3D Fourier space of the scattering potential. Equivalently, Eq. (22) states that point C in Fig. 3 on the Ewald surface of radius k_2 can be made to coincide with point B that resides on the Ewald surface of radius k_1 by rotating the former Ewald surface by an angle $-\phi''$ about the u axis. Equation (22) states also that point A on the Ewald surface of radius k_2 can be made to coincide with point D that resides on the Ewald surface of radius k_1 by rotating the former Ewald surface by an angle ϕ'' about the u axis.

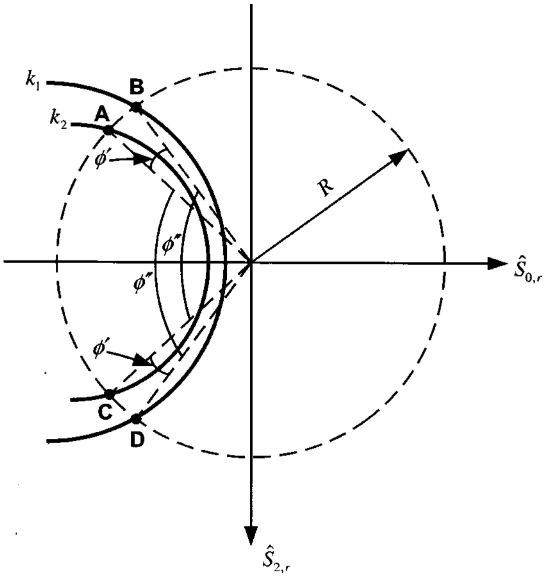

Fig. 3. Intersection of the hemispherical Ewald surfaces of radius k_1 and k_2 with a plane of constant u in the 3D Fourier space. The usefulness of this figure for interpreting Fourier space symmetries is explained in Subsection 3.B.

4. RECONSTRUCTION METHODS

Below we derive two multispectral I-DT reconstruction methods for use with quasi-nondispersive objects. The solution strategy is inspired by our recent study of spherical wave I-DT.[22] It involves exploitation of the Fourier space symmetries identified in Subsection 3.B and the rotational invariance of the problem.

A. Reconstruction Method 1

The data function $\hat{D}(u, v_r; d, \phi, \omega_1)$, which was defined in Eq. (15), evaluated at the frequencies (u, v_r') is given by

$$\begin{aligned}\hat{D}&(u, v_r'; d, \phi, \omega_1)\\ &= i\frac{\pi k_1^2}{\nu_1'}\{\hat{F}[u, v_r'; \phi, \omega_1]\exp[i(\nu_1' - k_1)d]\\ &\quad - (\hat{F}[-u, -v_r'; \phi, \omega_1])^*\exp[-i(\nu_1' - k_1)d]\},\end{aligned} \tag{24}$$

where ν_1' was defined in Eq. (21). On substitution from Eq. (17) into Eq. (24), one obtains

$$\begin{aligned}\hat{D}&(u, v_r'; d, \phi, \omega_1)\\ &= i\frac{\pi k_1^2}{\nu_1'}\{\hat{F}[u, v_r; \phi + \phi'(v_r), \omega_2]\exp[i(\nu_1' - k_1)d]\\ &\quad - (\hat{F}[-u, -v_r; \phi - \phi'(v_r), \omega_2])^*\exp[-i(\nu_1' - k_1)d]\},\end{aligned} \tag{25}$$

where the v_r dependence of ϕ' has been made explicit and we have used the fact that $\phi'(-v_r) = -\phi'(v_r)$. Similar to Eqs. (15) and (16), Eqs. (25) and (16) constitute a system of equations that relate the two intensity measurements on the detector plane $z_r = d$ at view angle ϕ to four distinct frequency components of $f(\mathbf{r})$. Note that the unknown frequency components in Eqs. (25) and (16) reside on Ewald surfaces that have a common radius k_2. However, due to the angular shifts $\pm\phi'$ in Eq. (25), the orientation of the surfaces is different. To circumvent this fact, we must exploit the rotational invariance of the problem.

Because $\hat{D}(u, v_r; d, \phi, \omega_j)$, with $j = 1, 2$, and $\hat{F}[u, v_r; \phi, \omega_2]$ are 2π periodic functions of ϕ, they can be expressed as the Fourier series

$$\hat{D}(u, v_r; d, \phi, \omega_j) = \sum_{n=-\infty}^{\infty} \hat{D}_n(u, v_r; d, \omega_j)\exp[in\phi], \tag{26}$$

$$\hat{F}[u, v_r; \phi, \omega_2] = \sum_{n=-\infty}^{\infty} \hat{F}_n[u, v_r; \omega_2]\exp[in\phi], \tag{27}$$

where

$$\hat{D}_n(u, v_r; d, \omega_j) = \frac{1}{2\pi}\int_0^{2\pi} \mathrm{d}\phi\, \hat{D}(u, v_r; d, \phi, \omega_j)\exp[-in\phi], \tag{28}$$

$$\hat{F}_n[u,v_r;\omega_2] = \frac{1}{2\pi}\int_0^{2\pi} \mathrm{d}\phi\, \hat{F}[u,v_r;\phi,\omega_2]\exp[-in\phi]. \tag{29}$$

Substitution from Eq. (25) into Eq. (28) results in

$$\begin{aligned}\hat{D}_n(u,v_r';d,\omega_1) &= i\frac{\pi k_1^2}{\nu_1'}\{\hat{F}_n[u,v_r;\omega_2]\exp[in\phi'(v_r) + i(\nu_1' - k_1)d] \\ &\quad - (\hat{F}_n[-u,-v_r;\omega_2])^* \exp[-in\phi'(v_r) - i(\nu_1' - k_1)d]\}.\end{aligned} \tag{30}$$

Similarly, on substitution from Eq. (16) into Eq. (28), one obtains

$$\begin{aligned}\hat{D}_n(u,v_r;d,\omega_2) &= i\frac{\pi k_2^2}{\nu_2}\{\hat{F}_n[u,v_r;\omega_2]\exp[i(\nu_2 - k_2)d] \\ &\quad - (\hat{F}_n[-u,-v_r;\omega_2])^* \exp[-i(\nu_2 - k_2)d]\}.\end{aligned} \tag{31}$$

Equations (30) and (31) represent a system of two equations involving the two unknowns $\hat{F}_n[u,v_r;\omega_2]$ and $(\hat{F}_n[-u,-v_r;\omega_2])^*$. The solution of this system yields

$$\hat{F}_n[u,v_r;\omega_2] = -i\frac{\nu_2}{\pi k_2^2}\exp[-i(\nu_2 - k_2)d]\frac{\hat{D}_n(u,v_r;d,\omega_2) - \left(\dfrac{k_2}{k_1}\right)^2\left(\dfrac{\nu_1'}{\nu_2}\right)\hat{D}_n(u,v_r';d,\omega_1)\exp[in\phi'(v_r) + i(\nu_1' - k_1 - \nu_2 + k_2)d]}{1 - \exp[2in\phi'(v_r) + 2i(\nu_1' - k_1 - \nu_2 + k_2)d]}. \tag{32}$$

Equations (32) and (27) together provide the desired method for reconstruction of $\hat{F}[u,v_r;\phi,\omega_2]$ for $u^2+v_r^2 \leqslant k_2^2$. From knowledge of these Fourier components, an estimate of $f(\mathbf{r})$ can be reconstructed by use of existing DT reconstruction algorithms.[19–21] Equation (32) contains isolated poles whose locations depend on the values of k_1 and k_2. Because $\hat{F}_n[u,v_r;\omega_2]$ can be determined up to a set of measure zero within the region of Fourier space defined by $u^2+v_r^2 \leqslant k_2^2$, these poles pose no mathematical difficulties. However, as discussed in Section 5, an explicit consideration of the poles must be taken when implementing the method numerically.

B. Reconstruction Method 2

An alternative reconstruction formula can be derived by use of the symmetries described in Eq. (22). Consider the data function $\hat{D}(u,v_r;d,\phi,\omega_1)$ [Eq. (15)] evaluated at the frequencies $(u,-v_r')$:

$$\begin{aligned}\hat{D}(u,-v_r';d,\phi,\omega_1) &= i\frac{\pi k_1^2}{\nu_1'}\{\hat{F}[u,-v_r';\phi,\omega_1]\exp[i(\nu_1' - k_1)d] \\ &\quad - (\hat{F}[-u,v_r';\phi,\omega_1])^* \exp[-i(\nu_1' - k_1)d]\}.\end{aligned} \tag{33}$$

By use of the symmetries given in Eq. (22), Eq. (33) can be expressed as

$$\begin{aligned}\hat{D}(u,-v_r';d,\phi,\omega_1) &= i\frac{\pi k_1^2}{\nu_1'}\{\hat{F}[u,v_r;\phi - \phi''(v_r),\omega_2]\exp[i(\nu_1' - k_1)d] \\ &\quad - (\hat{F}[-u,-v_r;\phi + \phi''(v_r),\omega_2])^*\exp[-i(\nu_1' - k_1)d]\}.\end{aligned} \tag{34}$$

On substitution from Eq. (34) into Eq. (28), one obtains

$$\begin{aligned}\hat{D}_n(u,-v_r';d,\omega_1) &= i\frac{\pi k_1^2}{\nu_1'}\{\hat{F}_n[u,v_r;\omega_2]\exp[-in\phi''(v_r) + i(\nu_1' - k_1)d] \\ &\quad - (\hat{F}_n[-u,-v_r;\omega_2])^*\exp[in\phi''(v_r) - i(\nu_1' - k_1)d]\}.\end{aligned} \tag{35}$$

Equations (35) and (31) represent a system of two equations involving the two unknowns $\hat{F}_n[u,v_r;\omega_2]$ and $(\hat{F}_n[-u,-v_r;\omega_2])^*$ whose solution yields

$$\hat{F}_n[u,v_r;\omega_2] = -i\frac{\nu_2}{\pi k_2^2}\exp[-i(\nu_2 - k_2)d]\frac{\hat{D}_n(u,v_r;d,\omega_2) - (k_2/k_1)^2(\nu_1'/\nu_2)\hat{D}_n(u,-v_r';d,\omega_1)\exp[-in\phi''(v_r) + i(\nu_1' - k_1 - \nu_2 + k_2)d]}{1 - \exp[-2in\phi''(v_r) + 2i(\nu_1' - k_1 - \nu_2 + k_2)d]}. \tag{36}$$

Equations (36) and (27) provide an alternative method for reconstruction of $\hat{F}[u,v_r;\phi,\omega_2]$ for $u^2+v_r^2 \leqslant k_2^2$. In a mathematical sense, the two reconstruction methods derived in this section are equivalent. Similar to Eq. (32), Eq. (36)

contains isolated poles whose locations depend on the values of k_1 and k_2. However, other than the pole at the origin of Fourier space, their locations are generally different. This indicates that the two reconstruction methods will generally propagate noise differently when applied to discretely sampled and inconsistent measurement data. A detailed investigation of the statistical properties of the reconstruction methods remains an interesting topic for future investigation. In the next section, a preliminary numerical investigation of the methods is provided.

5. NUMERICAL RESULTS

To demonstrate the proposed reconstruction methods, a computer simulation study for the 2D problem was conducted.

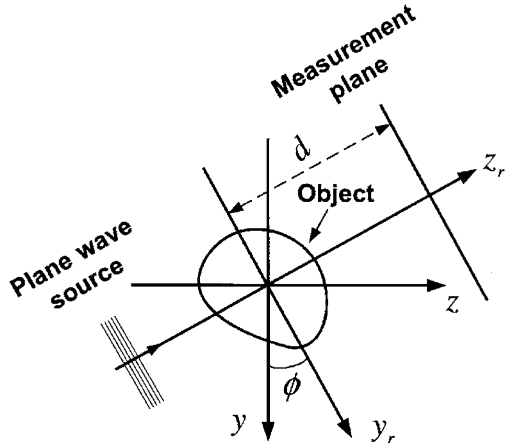

Fig. 4. Two-dimensional scanning geometry utilized in the computer simulation studies.

A. Scanning Geometry and Simulation Data

The assumed 2D tomographic scanning geometry is shown in Fig. 4. A probing plane wave propagates in the direction of the positive z_r axis, and the intensity of the forward-scattered wave field is recorded on a detector array placed a distance $d=1$ cm from the center of rotation. The detector array had a length of 1.024 cm and contained 1024 discrete elements. This corresponded to a detector pixel size of $\Delta y_r = 1.0 \times 10^{-5}$ m. At each view angle ϕ, two intensity measurements are recorded that correspond to different probing plane waves that have wavelengths $\lambda_1 = 0.5 \times 10^{-5}$ m and $\lambda_2 = 0.68 \times 10^{-5}$ m, or equivalently, wavenumbers $k_1 = 1.26 \times 10^6$ m^{-1} and $k_2 = 0.92 \times 10^6$ m^{-1}. The angular scanning consisted of sampling ϕ at 360 view angles that were evenly spaced over the interval $[0, 2\pi)$.

The real and imaginary components of the object's complex-valued refractive index distribution were represented by the mathematical phantom shown in Figs. 5(a) and 5(b), respectively. The length of the major and minor axes of the largest ellipse (i.e., the background ellipse) was 0.92 and 0.62 mm, respectively. The refractive index values in the phantom are indicated in the profile plots in Figs. 5(c) and 5(d). From knowledge of $n(\mathbf{r})$, the complex phases $\psi(y_r; d, \phi, \omega_1)$ and $\psi(y_r; d, \phi, \omega_2)$ were calculated analytically[22] and the measured intensity data $I(y_r; d, \phi, \omega_1)$ and $I(y_r; d, \phi, \omega_2)$ were formed according to Eq. (4) (with the x dependence omitted). In generating the data in this manner, we assumed that the first Rytov approximation is valid[23] and that $n(\mathbf{r}, \omega_1) = n(\mathbf{r}, \omega_2)$. The potential effects of violating the latter assumption are discussed in Section 6. Noisy versions of the intensity data

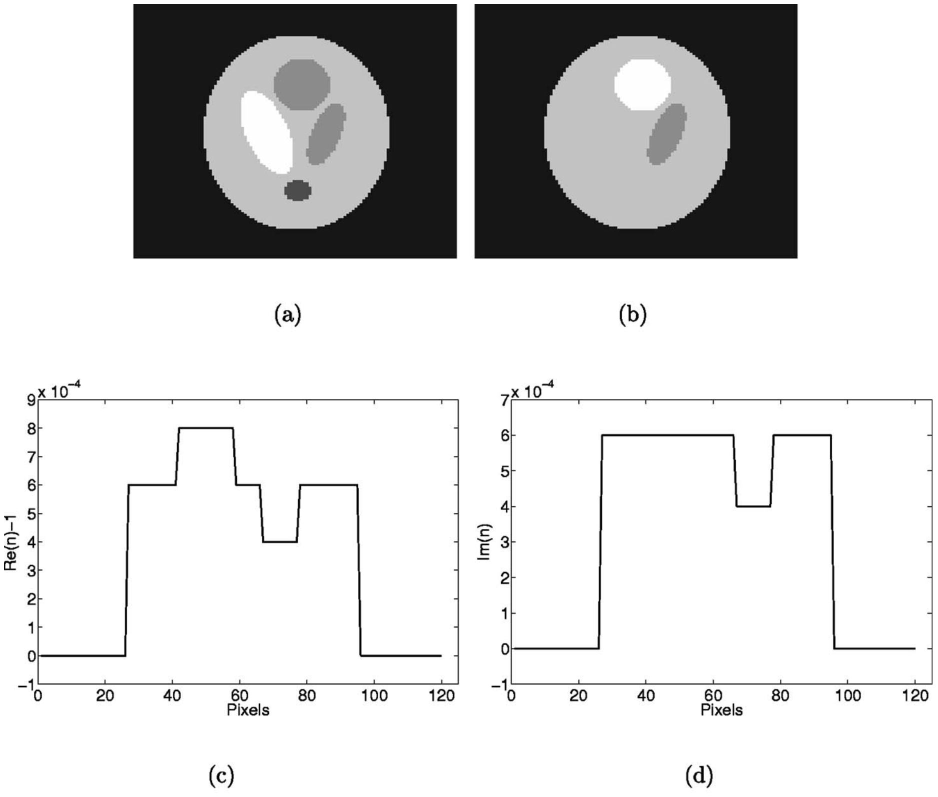

(a) (b)

(c) (d)

Fig. 5. Mathematical phantom object that represents (a) $\mathrm{Re}\{n(\mathbf{r})\} - 1$ and (b) and $\mathrm{Im}\{n(\mathbf{r})\}$. (c) Profile through the central row in (a). (d) Profile through the central row in (b).

were generated as realizations of uncorrelated Gaussian stochastic processes that were characterized by their means μ and standard deviations σ. When generating the noisy data, μ was set equal to the noiseless value of $I(y_r;d,\phi,\omega_{j=1,2})$ at a given detector location and σ was chosen to satisfy $\sigma/\mu=0.4\%$.

B. Reconstruction Procedure

Reconstruction methods 1 and 2 described in Section 4 were implemented numerically as follows. The logarithm of the intensity data $I(y_r;d,\phi,\omega_1)$ and $I(y_r;d,\phi,\omega_2)$ was computed to form the intensity data functions $D(y_r;d,\phi,\omega_1)$ and $D(y_r;d,\phi,\omega_2)$ as prescribed by Eq. (5), and their one-dimensional (1D) Fourier transforms $\hat{D}(v_r;d,\phi,\omega_1)$ and $\hat{D}(v_r;d,\phi,\omega_2)$ were computed by use of the fast-Fourier-transform (FFT) algorithm. (Here and elsewhere, the u dependence of the equations will be omitted in this 2D example.) From the set of uniformly spaced values of v_r at which these functions were evaluated, the set of nonuniformly spaced values v_r' was computed by use of Eq. (18). The values of $\hat{D}(v_r';d,\phi,\omega_1)$ and $\hat{D}(-v_r';d,\phi,\omega_1)$ were determined by first increasing the sampling density of the uniformly spaced data $\hat{D}(v_r;d,\phi,\omega_1)$ by a factor of 16 via zero padding in the spatial domain,[24] followed by a linear interpolation operation. The Fourier series expansion coefficients $\hat{D}_n(v_r';d,\omega_1)$, $\hat{D}_n(-v_r';d,\omega_1)$, and $\hat{D}_n(v_r;d,\omega_2)$ were calculated subsequently by use of the 1D FFT algorithm.

Reconstruction method 1 described in Subsection 4.A was implemented, where Eq. (32) was employed for estimation of $\hat{F}_n[u,v_r;\omega_2]$. A simple regularization strategy was utilized to mitigate the effects of the singularities in the reconstruction formula. Let $D_n(v_r)$ denote the denominator of Eq. (32). Equation (32) was utilized to estimate $F_n[v_r;\omega_2]$ only for the frequency components v_r such that $|D_n(v_r)|\geq\epsilon$, where ϵ is a threshold parameter that was set at the value of 0.001. For the frequency components where $|D_n(v_r)|<\epsilon$, i.e., at or near the locations of singularities in Eq. (32), the value of $F_n[v_r;\omega_2]$ was set to zero. The Fourier data $\hat{F}[v_r;\phi,\omega_2]$ were then computed by application of the 1D inverse FFT algorithm to $F_n[v_r;\omega_2]$. Finally, from $\hat{F}[v_r;\phi,\omega_2]$, an estimate of $f(\mathbf{r})$ was obtained by use of the DT reconstruction algorithm that is described in Refs. 20 and 25. Reconstruction method 2 given in Subsection 4.B was implemented in an analogous fashion. In that case, Eq. (36) was employed for estimation of $F_n[v_r;\omega_2]$. Both reconstruction methods were utilized for reconstruction of images from the noiseless and noisy data sets described in Subsection 5.A. The matrix size of the reconstructed images was 120 × 120 pixels.

C. Reconstructed Images

Figure 6 contains images of the refractive index distribution reconstructed from the noiseless simulation data by use of reconstruction methods 1 and 2. The images in Figs. 6(a) and 6(b) correspond to $\mathrm{Re}\{n(\mathbf{r})\}-1$ and $\mathrm{Im}\{n(\mathbf{r})\}$, respectively, reconstructed by use of method 1. Here, $\mathrm{Re}\{\cdot\}$ and $\mathrm{Im}\{\cdot\}$ denote the real and imaginary components, respectively, of a complex-valued function. Image profiles through the central rows of Figs. 6(a) and 6(b) are displayed in Figs. 7(a) and 7(b), respectively, which are superimposed on the true phantom profiles. These profiles confirm that the phantom is reconstructed with high fi-

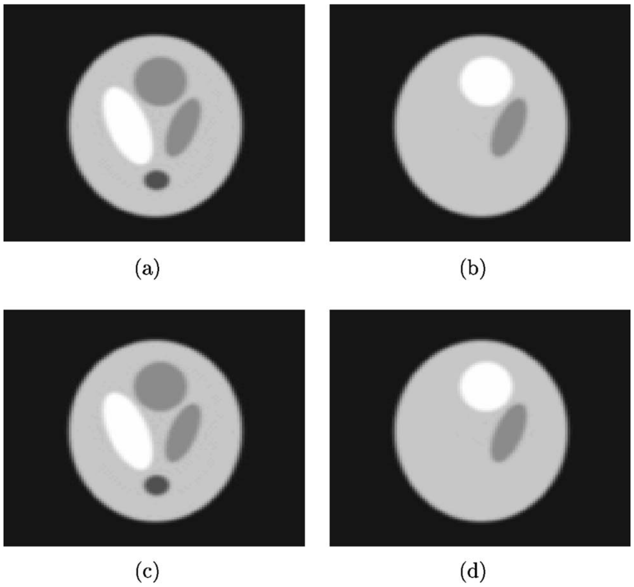
(a) (b)

(c) (d)

Fig. 6. Images of (a) $\mathrm{Re}\{n(\mathbf{r})\}-1$ and (b) $\mathrm{Im}\{n(\mathbf{r})\}$ reconstructed from the noiseless simulation data by use of method 1. The corresponding images reconstructed by use of method 2 are shown in (c) and (d).

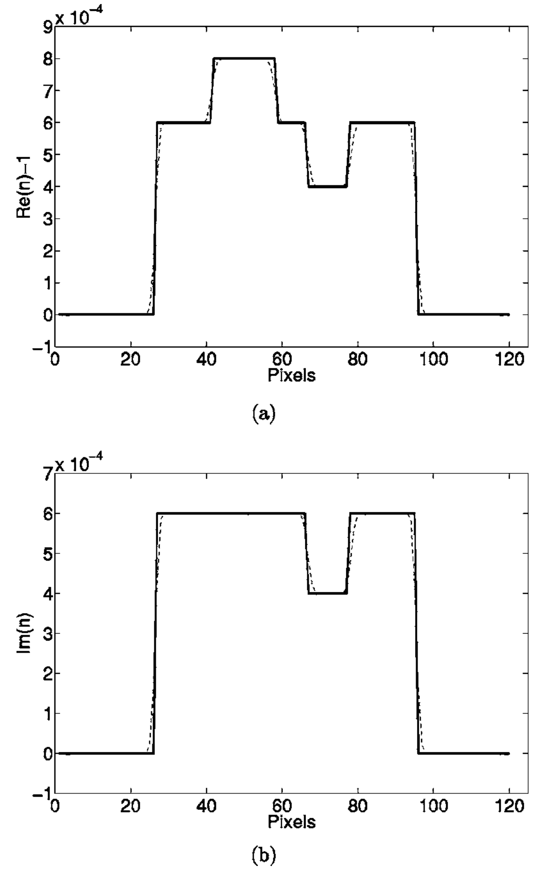

Fig. 7. Dashed curves in (a) and (b) display profiles through the central rows of Figs. 6(a) and 6(b), respectively. In each case, the profile through the true phantom is represented by a solid line.

delity from the noiseless data. Noiseless images reconstructed by use of method 2 are shown in Figs. 6(c) and 6(d), and are virtually identical to the images reconstructed by use of method 1.

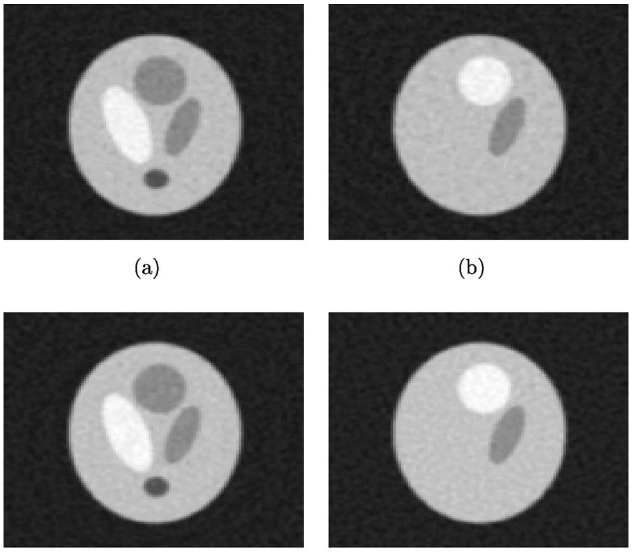
(a) (b)

(c) (d)

Fig. 8. Images of (a) $\mathrm{Re}\{n(\mathbf{r})\}-1$ and (b) $\mathrm{Im}\{n(\mathbf{r})\}$ reconstructed from the noisy simulation data by use of method 1. The corresponding images reconstructed by use of method 2 are shown in (c) and (d).

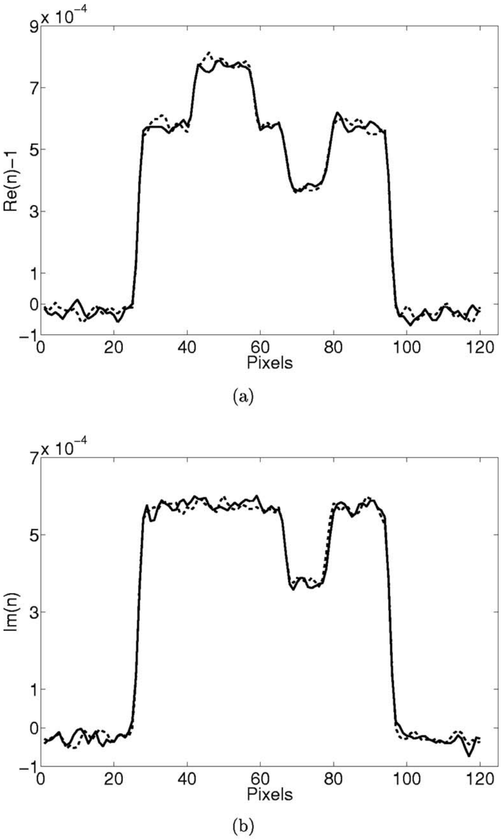

Fig. 9. (a) Profiles through the central rows of Figs. 8(a) and 8(c) are represented by the solid and dashed curves, respectively. (b) Profiles through the central rows of Figs. 8(b) and 8(d) are represented by the solid and dashed curves, respectively.

Figure 8 contains images of the refractive index distribution reconstructed from the noisy simulation data by use of reconstruction methods 1 and 2. The images in Figs. 8(a) and 8(b) correspond to $\mathrm{Re}\{n(\mathbf{r})\}-1$ and $\mathrm{Im}\{n(\mathbf{r})\}$, respectively, reconstructed by use of method 1. The corresponding images reconstructed by use of method 2 are shown in Figs. 8(c) and 8(d). The image profiles through the central rows of Figs. 8(a) and 8(c) are represented by the solid and dashed curves, respectively, in Fig. 9(a), while the corresponding profiles through the central rows of Figs. 8(b) and 8(d) are contained in Fig. 9(b). The fact that the noisy images reconstructed by use of the different methods are distinct is to be expected. It is well known that, even if equivalent mathematically, different tomographic reconstruction algorithms will generally propagate noise and other data inconsistencies in different ways.[20,26]

6. DISCUSSION AND SUMMARY

Conventional I-DT requires measurements of the wave field intensities on two different parallel detector planes at each tomographic view angle. In this work, a multispectral I-DT reconstruction theory for quasi-nondispersive scattering objects was developed and investigated. By quasi-nondispersive, we refer to an object that is characterized by a refractive index distribution that is approximately independent of temporal frequency over a defined finite closed interval. For such objects, we demonstrated that two intensity measurements acquired on a single detector plane at each view angle can provide sufficient information for image reconstruction. This requires a scanning geometry in which the two intensity measurements are generated by probing plane waves that have distinct temporal frequencies that reside within an interval where object dispersion can be neglected. Accordingly, the frequency of the probing wave field can be varied for acquisition of the necessary measurement data rather than the detector position as required in conventional I-DT. This alternative data-acquisition strategy may have significant practical advantages in certain imaging studies.

It is interesting to note that the general mathematical structure of our analysis and reconstruction methods is the same as employed in our previous study of spherical wave I-DT.[22] Although the scanning geometries and physical assumptions employed in these works differ, their interpretations from a Fourier space perspective are remarkably similar. In both cases, the measurement data at each tomographic view angle are found to specify systems of two equations with four unknowns, where the unknowns represent distinct Fourier components of the scattering potential. In both cases, the development of reconstruction methods is facilitated by the identification of Fourier space data symmetries and the use of Fourier series expansions to exploit the rotational invariance of the imaging models.

There remain several important topics for future investigations. A key assumption of our methods is that the object can be regarded as dispersionless over the temporal frequency window in which the intensity measurements are acquired. In cases where this assumption is not valid, the measurement data will necessarily be inconsistent with the assumed imaging model. The degree to which artifacts due to data inconsistencies can be mitigated by the proposed reconstruction methods requires further study. Another important topic of investigation is the extension of the methods to utilize measurements corresponding to more than two temporal frequencies. When such additional measurements are available, they can, in principle, be utilized to improve the noise characteristics of the reconstructed images. It would also be useful to generalize the methods for use with dispersive objects with known dispersion laws.

APPENDIX A

In this appendix we establish the Fourier space symmetry properties described by Eqs. (17) and (22). Consider Fig. 3, which shows the intersection of Ewald surfaces of radii k_1 and k_2 with a plane of constant u. The 3D locations of points A and C that reside on the surface with radius k_2 are given by

$$\mathbf{K}_A(\phi) = u\mathbf{s}_1 - v_r\mathbf{s}_{2,r}(\phi) + (\nu_2 - k_2)\mathbf{s}_{0,r}(\phi),$$

$$\mathbf{K}_C(\phi) = u\mathbf{s}_1 + v_r\mathbf{s}_{2,r}(\phi) + (\nu_2 - k_2)\mathbf{s}_{0,r}(\phi).$$

The argument ϕ in $\mathbf{K}_A(\phi)$ and $\mathbf{K}_B(\phi)$ denotes that the vectors $\mathbf{K}_A$ and $\mathbf{K}_B$ are expressed in the rotated coordinate system. The distance between these points and the origin of the plane of constant u is given by

$$\begin{aligned} R &= |\mathbf{K}_C - (\mathbf{K}_C \cdot \mathbf{s}_1)\mathbf{s}_1| = |v_r\mathbf{s}_{2,r}(\phi) + (\nu_2 - k_2)\mathbf{s}_{0,r}(\phi)| \\ &= [v_r^2 + (\nu_2 - k_2)^2]^{1/2}, \end{aligned}$$

which coincides with Eq. (19).

The locations of points B and D in Fig. 3 that reside on the Ewald surface with radius k_1 are given by

$$\mathbf{K}_B(\phi) = u\mathbf{s}_1 - v_r'\mathbf{s}_{2,r}(\phi) + (\nu_1' - k_1)\mathbf{s}_{0,r}(\phi),$$

$$\mathbf{K}_D(\phi) = u\mathbf{s}_1 + v_r'\mathbf{s}_{2,r}(\phi) + (\nu_1' - k_1)\mathbf{s}_{0,r}(\phi),$$

where $v_r' \geqslant 0$. Because points A, B, C, and D all reside on the same circle of radius R in the plane of constant u, the coordinate v_r' must satisfy

$$R^2 = v_r'^2 + (\nu_1' - k_1)^2 = v_r'^2 + (\sqrt{k_1^2 - u^2 - v_r'^2} - k_1)^2. \quad \text{(A1)}$$

Equation (A1) can be simplified as

$$(R^2 + u^2)^2 + 4k_1^2(v_r'^2 - R^2) = 0,$$

whose solution indicates that

$$v_r' = \left[R^2 - \frac{(R^2 + u^2)^2}{4k_1^2}\right]^{1/2}.$$

Since we assume $k_1 > k_2$, it can be verified that for $u^2 + v_r^2 \leqslant k_2^2$ the solution is real valued.

From the definition of ϕ' in Eq. (20), one finds that

$$\mathbf{K}_A(\phi + \phi') = \mathbf{K}_B(\phi), \quad \mathbf{K}_C(\phi + \phi') = \mathbf{K}_D(\phi), \quad \text{(A2)}$$

which establishes the symmetries given in Eq. (17). Note that from Eq. (20), $\phi' < 0$ in the former identity in Eqs. (A2), while $\phi' > 0$ in the latter. From the definition of ϕ'' in Eq. (23), one finds that

$$\mathbf{K}_A(\phi - \phi'') = \mathbf{K}_D(\phi), \quad \mathbf{K}_C(\phi - \phi'') = \mathbf{K}_B(\phi), \quad \text{(A3)}$$

which establishes the symmetries given in Eq. (22). Note that from Eq. (23), $\phi'' < 0$ in the former identity in Eqs. (A3), while $\phi'' > 0$ in the latter.

Corresponding author M. Anastario's e-mail address is anastasio@iit.edu.

REFERENCES

1. E. Wolf, "Principles and development of diffraction tomography," in *Trends in Optics*, A. Consortini, ed. (Academic, 1996), pp. 83–110.
2. A. J. Devaney, "Reconstructive tomography with diffracting wavefields," Inverse Probl. **2**, 161–183 (1986).
3. T. C. Wedberg and J. J. Stamnes, "Recent results in optical diffraction microtomography," Meas. Sci. Technol. **7**, 414–418 (1996).
4. T. Wedberg and J. Stamnes, "Quantitative imaging by optical diffraction tomography," Opt. Rev. **2**, 28–31 (1995).
5. V. Lauer, "New approach to optical diffraction tomography yielding a vector equation of diffraction tomography and a novel tomographic microscope," J. Microsc. **205**, 165–176 (2001).
6. A. S. T. Beetz and C. Jacobsen, "Soft x-ray diffraction tomography: simulations and first experimental results," J. Phys. (Paris) **104**, 31–34 (2003).
7. M. A. Anastasio and D. Shi, "On the relationship between intensity diffraction tomography and phase-contrast tomography," in *Developments in X-ray Tomography IV*, U. Bonse, ed., Proc. SPIE **5535**, 361–368 (2004).
8. P. Grassin, B. Duchene, and W. Tabbara, "Diffraction tomography: some applications and extension to 3-d ultrasound imaging," in *Mathematical Methods in Tomography* (Springer-Verlag, 1991), pp. 98–105.
9. T. Mast, "Wideband quantitative ultrasonic imaging by time-domain diffraction tomography," J. Acoust. Soc. Am. **106**, 3061–3071 (1999).
10. D. Shi, M. A. Anastasio, Y. Huang, and G. Gbur, "Half-scan and single-plane intensity diffraction tomography for phase objects," Phys. Med. Biol. **49**, 2733–2752 (2004).
11. G. Gbur, M. A. Anastasio, Y. Huang, and D. Shi, "Spherical-wave intensity diffraction tomography," J. Opt. Soc. Am. A **22**, 230–238 (2005).
12. G. Gbur and E. Wolf, "Diffraction tomography without phase information," Opt. Lett. **27**, 1890–1892 (2002).
13. G. Gbur and E. Wolf, "Hybrid diffraction tomography without phase information," J. Opt. Soc. Am. A **19**, 2194–2202 (2002).
14. M. R. Teague, "Deterministic phase retrieval: a Green's function solution," J. Opt. Soc. Am. **73**, 1434–1441 (1983).
15. A. Barty, K. A. Nugent, A. Roberts, and D. Paganin, "Quantitative phase tomography," Opt. Commun. **175**, 329–336 (2000).
16. Y. Waseda, *Novel Application of Anomalous (Resonance) X-ray Scattering for Structural Characterization of Disordered Materials* (Springer-Verlag, 1984).

17. G. Gbur and E. Wolf, "Determination of density correlation functions from scattering of polychromatic light," Opt. Commun. **168**, 39–45 (1999).
18. P. S. Carney and J. C. Schotland, "Inverse scattering for near-field microscopy," Appl. Phys. Lett. **77**, 2798–2800 (2000).
19. M. A. Anastasio and X. Pan, "Computationally efficient and statistically robust image reconstruction in 3D diffraction tomography," J. Opt. Soc. Am. A **17**, 391–400 (2000).
20. X. Pan, "A unified reconstruction theory for diffraction tomography with considerations of noise control," J. Opt. Soc. Am. A **15**, 2312–2326 (1998).
21. A. J. Devaney, "A filtered backpropagation algorithm for diffraction tomography," Ultrason. Imaging **4**, 336–350 (1982).
22. M. A. Anastasio, D. Shi, Y. Huang, and G. Gbur, "Image reconstruction in spherical wave intensity diffraction tomography," J. Opt. Soc. Am. A **22**, 2651–2661 (2005).
23. B. Chen and J. Stamnes, "Validity of diffraction tomography based on the first Born and first Rytov approximations," Appl. Opt. **37**, 2996–3006 (1998).
24. S. Pan and A. Kak, "A computational study of reconstruction algorithms for diffraction tomography: interpolation versus filtered backpropagation," IEEE Trans. Acoust. Speech Signal Process. **31**, 1262–1275 (1983).
25. M. A. Anastasio and X. Pan, "Investigation of the noise properties of a new class of reconstruction methods in diffraction tomography," Int. J. Imaging Syst. Technol. **10**, 437–446 (1999).
26. E. Clarkson, "Projections onto the range of the exponential Radon transform and reconstruction algorithms," Inverse Probl. **15**, 563–571 (1999).